Journal of Engineering Science and Technology
Vol. 20, No. 4 (2025) 1012 - 1025

AERODYNAMIC ANALYSIS OF PLAIN FLAP INTEGRATION IN VERTICAL AXIS WIND TURBINES USING CFD AT DIFFERENT TIP SPEED RATIOS

ZULFAQAR ZAHARI[1], MOHAMAD SHUKRI ZAKARIA[1,*], HASLINA ABDULLAH[2], ADI AZRIFF BASRI[3], MOHD JUZAILA ABD LATIF[1]

[1]Fakulti Teknologi Kejuruteraan Mekanikal, Universiti Teknikal Malaysia Melaka, Hang Tuah Jaya, 76100 Durian Tunggal, Melaka, Malaysia
[2]Faculty of Mechanical and Manufacturing Engineering, Universiti Tun Hussein Onn Malaysia, 86400 Parit Raja, Batu Pahat, Johor, Malaysia
[3]Department of Aerospace Engineering, Universiti Putra Malaysia, Serdang 43400, Malaysia
*Corresponding Author: mohamad.shukri@utem.edu.my

Abstract

This study was aimed at enhancing the performance of a vertical axis wind turbine, by incorporating a plain flap at the trailing edge of a NACA 0015 aerofoil blade. The performance of the vertical axis wind turbine was analysed by solving the two-dimensional Unsteady Reynolds-Averaged Navier-Stokes equations. The effect of the plain flap on the performance of the vertical axis wind turbine was evaluated at Reynolds Number of 1.7×10^6. Computational fluid dynamics simulations were used to compare the power coefficients and vorticity magnitudes of the aerofoil at various tip speed ratios of 1.5, 2.0, 2.5, and 3.0, both with and without the plain flap. For each tip speed ratio, the observed pressure coefficient increment was 15.32%, 16.49%, 9.97%, and 19.42%. The results indicated a significant improvement of up to 20% in the pressure coefficient with the addition of the flap compared to the clean aerofoil, thereby suggesting its potential to enhance energy efficiency in vertical axis wind turbines. A Flow visualisation also demonstrated that the flap reduced vortex formation and improved flow attachment. The study concluded that the plain flap design significantly boosts aerodynamic efficiency, and further optimisation recommends exploiting its benefits fully. Future research could explore adaptive flap designs and real-world implementations under varying wind conditions to further enhance the wind turbine efficiency and stability.

Keywords: Aerodynamics, Computational fluid dynamics, Tip speed ratio wind turbine.

1. Introduction

Vertical axis wind turbines (VAWTs) offer several advantages over horizontal axis wind turbines (HAWTs), such as the ability to harness wind from any direction, easy maintenance, smaller footprint and a simpler mechanical design. However, they often suffer from lower efficiency and more complex flow phenomena, including dynamic stall, which leads to fluctuating torque and reduced performance [1]. These challenges lead to reduced power output and limit their viability in large-scale wind energy applications.

Addressing these issues is crucial to unlock the potential of VAWTs as a competitive renewable energy solution. Traditional efforts to enhance the performance of VAWTs have focused on optimising the blade shape and turbine configuration, yet these approaches have failed to fully address the aerodynamic challenges inherent in VAWTs. Among the various modifications explored, the incorporation of flaps has shown considerable potential in mitigating some of these challenges by improving lift and reducing drag, thereby stabilising the torque output [2].

In aeronautical engineering, it is a well-established fact that flaps are important for increasing lift during critical phases such as take-off and landing. In the context of VAWTs, flaps can dynamically optimise the angle of attack, leading to improved aerodynamic performance. Hao and Li [3] demonstrated that the strategic deployment of flaps can significantly increase the power coefficient (C_p), particularly during critical phases of blade rotation. These improvements will translate into higher energy capture and a smoother T output, effectively addressing some of the inefficiencies observed in VAWT designs.

However, despite these promising results, the application of flaps to VAWTs remains underexplored. While flaps can enhance lift, they may also reduce the C_p if not optimally designed or controlled, potentially offsetting the expected efficiency gains, especially at lower tip speed ratios (TSRs). This trade-off underscores the need for further research to optimise flap designs, specifically for VAWTs.

The choice of tip speed ratio (TSR) significantly impacts aerodynamic efficiency, torque output, and dynamic stability. Low TSRs (e.g., 1.0-2.0) are typically associated with reduced efficiency due to increased dynamic stall and flow separation, whereas high TSRs (e.g., >3.0) can result in excessive vortex shedding and aerodynamic losses. Studies such as Hao and Li [3] have highlighted that optimizing TSR is crucial for balancing lift-to-drag ratios and minimizing energy losses. The present work contributes to this field by evaluating the effects of plain flaps at TSRs ranging from 1.5 to 3.0, offering insights into how flap-induced flow control mechanisms can improve efficiency across varying TSR ranges.

Computational Fluid Dynamics (CFD) has been applied in numerous engineering fields, including automotive [4], biomedical [5], heat transfer [6], oil and gas [7], and many more. While CFD modelling in aerodynamics applications is common [8], the potential for power improvement through novel aerofoil modifications is promising [9]. The potential of flaps to improve the performance of VAWTs has been further supported by CFD studies [10].

Jin et al. [11] conducted simulations on a Darrieus-type VAWT and found that passive flaps can significantly enhance lift while mitigating dynamic stall, resulting in a more stable torque output. Similarly, Hao et al. [12] explored various flap

configurations and identified optimal flap angles that can lead to substantial power output improvements, particularly at low TSRs, where VAWTs typically underperform.

This study aimed to investigate the influence of plain flaps on the C_p of VAWTs at various TSRs of the NACA0015 aerofoil. The focus key parameters are power coefficient (Cp), vorticity magnitude, torque output, and flow dynamics across various tip speed ratios (TSRs), by addressing critical challenges like fluctuating torque and flow separation. The originality of this work lies in its comprehensive approach to modelling and analysing the effects of flaps on VAWTs.

This study introduces a novel application of plain flaps in VAWT design to address inefficiencies at varying TSRs. Unlike earlier works (such as Hao et al. [12]) that primarily focused on flap angles, this study examines the aerodynamic effects of flap length and placement, hypothesizing improvement in power coefficient (Cp) across all TSRs. This study will offer new insights that could lead to more efficient VAWT designs, particularly in low-wind speed environments. Moreover, the research will provide a validated CFD methodology that can be used in future studies, thus bridging the gap between theoretical analyses and practical applications in wind turbine designs.

2. Methods

2.1. Geometry and meshing

In this study, the standard NACA 0015 aerofoil geometry was utilized as a turbine blade profile with a chord length, C of 0.4 m, similar clean profile used by Zhang et al. [13]. The NACA 0015 was chosen due to its symmetrical design, moderate thickness (15% of the *C*), predictable stall characteristics, and suitability for varying angles of attack [12]. Its extensive experimental data and use in prior research make it ideal for benchmarking and validation.

Figure 1(a) presents the solid model of the NACA 0015 aerofoil in its clean state, while Fig. 1(b) displays the modified version with a plain flap. The dimensions of the plain flap that was added to the aerofoil are shown in Fig. 1(c). The flap extended to over 15% of the *C*, overlapping the aerofoil by 12% of the *C*. Additionally, the thickness of the flap measured at the trailing edge was 4% of the *C*.

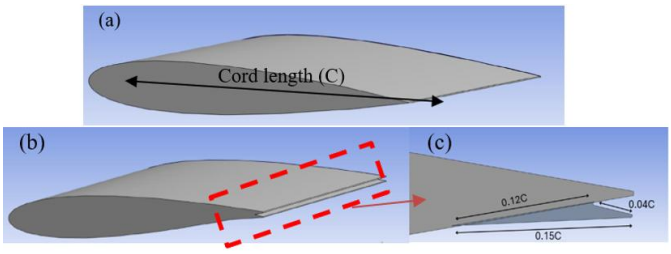

Fig. 1. The geometries of the (a) clean aerofoil, (b) plain flap aerofoil, and (c) close-up dimensions of the flap.

The dimensions of the rectangular-shaped domain were set to be 15 times greater than the *C* of the aerofoil, with a distance of 10*C* from the trailing edge to the open boundary. The distance between the inlet and the rotating shaft was 5*C*,

and the diameters of the two circles encompassing the rotating aerofoil were 3.1 m and 1.9 m, respectively.

A hybrid mesh was used, with tetrahedral elements applied far from the aerofoil and hexahedral elements near the aerofoil wall. The mesh was refined in critical areas, particularly around the leading and trailing edges of the turbine blade, where high pressure and velocity gradients were expected. A finer mesh was also applied within the rotating zone to better resolve the interaction between the rotating blade and the surrounding air.

A computational domain was created separately for the rotating zone and stationary zone to accurately capture the aerodynamic characteristics of the turbine blade. The mesh near the blade surface was refined to ensure an adequate boundary layer resolution. This was achieved by using multiple layers of inflation near the blade surface, ensuring that the $y+$ values of the wall were within the acceptable range for accurate turbulence modelling. Figure 2 shows the domain and meshing setups for the model.

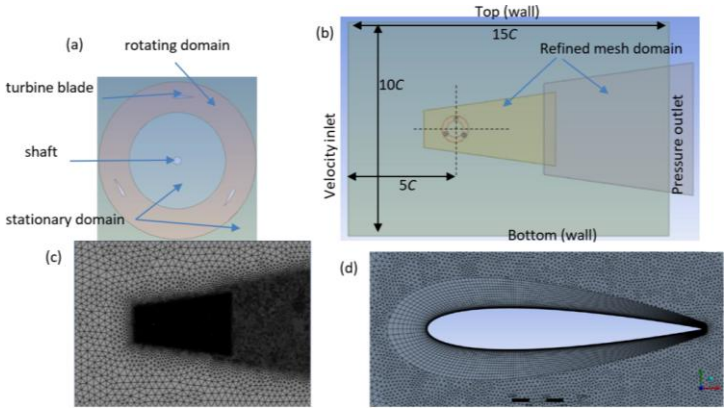

Fig. 2. Pre-processing stages of the model shows the (a) domain, (b) boundary condition, (c) overall meshing view with high density around the aerofoil and wake region, and (d) meshing view near the aerofoil boundary.

The inflation layer was applied to these aerofoils, with the thickness of the first layer set to 5×10^{-6} m and a maximum of 30 layers to target a y^+ of around one, fully resolving the boundary layer in the CFD simulations. The first layer thickness, Δy was calculated from y^+, as in Eq. (1).

$$\Delta y = \frac{y^+ \mu}{u_t \rho} \tag{1}$$

where u_t is friction velocity, ρ is density and μ is the viscosity of the fluid.

2.2. Mathematical model

A commercial CFD code ANSYS Fluent 2022R2 was used to solve the set of governing equations. The three-dimensional, incompressible, and steady governing equation consisted of a continuity and Navier-Stokes equations in three dimensions, and an energy equation, as given in Eqs. (2) and (3):

Continuity Equation:

$$\nabla \cdot U = 0 \tag{2}$$

Momentum Equation:

$$(U \cdot \nabla)U = -\frac{1}{\rho}\nabla p + \upsilon \nabla^2 U \tag{3}$$

where U is the velocity vector, and ρ and ν are density and viscosity, respectively.

The Reynolds-averaged Navier-Stokes Equations, with the *k-ω* turbulence model, were used to simulate the turbulence flow because they result in stable calculations that converge relatively easily, and their predictions of many flows are reasonable. The *k−ω* shear stress transport (SST) turbulence model is considered suitable for most engineering applications. The transport equations for the *k-ω* SST turbulence model are given in Eqs. (4) and (5).

Transport equation for turbulent kinetic energy (*k)*:

$$\frac{\partial(\rho k)}{\partial t} + \nabla \cdot (\rho U k) = \nabla \cdot \left(\left(\mu + \frac{\mu_t}{\sigma_k} \right) \nabla k \right) + P_k - \rho \varepsilon \tag{4}$$

Transport equation for specific turbulent dissipation rate (*ω)*:

$$\frac{\partial(\rho \omega)}{\partial t} + \nabla \cdot (\rho U \omega) = \nabla \cdot \left(\left(\mu + \frac{\mu_t}{\sigma_k} \right) \nabla \omega \right) + \frac{\gamma}{\nu_t} P_k - \beta \rho \omega^2 \tag{5}$$

The details of the SST model can be found in Sparrow et al. [14], among others.

After over 1000 iterations of the simulations were executed on a W-2255 Intel® Xeon processor with 128 GB of random-access memory (RAM), the convergence residual remained stable. Nevertheless, a tight convergence criterion, with a root mean square of 1.0×10^{-5}, was applied to the computational variables, including continuity, velocity, turbulence, specific dissipation rate, and the energy equations for all the case studies.

Equation (6) provides the C_p:

$$C_p = \frac{T\omega}{0.5\rho v^3 A_s} \tag{6}$$

where ρ is a density of 1.225 kg/m^3; v is a wind speed of 10m/s, which was applied to the various TSRs; and the sweep area is A_s=D×H, with D corresponding to the diameter of the VAWT's rotor or turbine [13] and H its height. As the analysis was conducted in 2D, the H was taken as one unit. T is the torque and ω is the angular velocity (rad/s), which was calculated using Eq. (7):

$$\omega = \frac{2\times TSR}{vD} \tag{7}$$

Therefore, for the TSRs of 1.5, 2.0, 2.5, and 3.0 that were examined in this study, the corresponding ω were 12, 14, 20, and 24 rad/s, respectively.

2.3. Boundary condition and material properties

A rectangular domain was constructed to enclose the aerofoil, and a velocity of 10 m/s was applied at the inlet, while a pressure outlet of zero was set at the outlet boundary. Slip conditions with zero shear were applied at the top and bottom boundaries. Non-slip conditions were set for the turbine blade and shaft. The middle

domain was set to rotate with a mesh motion of ω = 20 rad/s in a counter-clockwise direction. For the material properties, the density and viscosity were 1.225 kg/m³ and 1.7894×10^{-5} kg/(m·s) [13]. The Reynolds number was calculated using the formula $Re = \rho UD/v$, where D = 2.5 m. The other quantities were defined beforehand, resulting in a calculated Reynolds number of 1.7×10^{6}.

The timestep size, ΔT was chosen to enable the turbine to rotate by 1° in one timestep number. The timestep size was estimated using Eq. (8):

$$\Delta T = \frac{\text{Time to complete 1 revolution}}{360} = \frac{2\pi/\omega}{360} \tag{8}$$

As can be seen, the timestep size was dependent on the ω and, thus, the TSR. Therefore, for TSRs of 1.5, 2.0, 2.5, and 3.0, the timestep sizes were 1.4546, 1.0910, 0.8728, and 0.7273 ms, respectively. Although the timestep sizes were different for the T measurement, the results of the 360 timesteps were averaged for consistency.

2.4. Verification and validation of the model

The method used in the present study was validated using the experimental and numerical work of Zhang et al. [13] (Table 1). The case for TSR = 2.5 was chosen. The numerical result for the C_p showed a sufficiently low error of 5% compared to the previous experimental work, proving that the present study was well-validated.

Table 1. A comparison of the power coefficient (C_p) at TSR=2.5.

	Power Coefficient (C_p)	Error (%)
Zhang et al. [13] Experiment	0.317	-
Zhang et al. [13] CFD	0.345	8.81
Present CFD (SST k-ω)	0.301	5.05

The verification process quantified the discretisation error and was conducted through a grid independence study. For each model, three grid sizes were implemented, namely coarse, medium, and fine (Table 2). The refinement ratio (r) between the grids was 1.35 and 1.40, which were larger than 1.3, as proposed by Celik et al. [15]. The simulations were conducted under identical conditions across these grids, and the C_p was calculated for each. The representative cell length (h) was calculated as:

$$h = \left[\frac{1}{N}\sum_{i=1}^{N}(\Delta V_i)\right]^{1/3} \tag{9}$$

where N is the grid number and ΔA_i is the area for the i^{th} cells.

Table 2. the results of the grid convergence index (GCI) analysis.

Mesh	Element Number	Representative cell length ($\times10^{-2}$)	Grid ratio	Power Coefficient (C_p)	Relative error
Fine (N2)	137489	h_1=1.93	r_{21}=1.35	0.301	2.33%
Medium (N2)	55473	h_2=2.62	r_{32}=1.40	0.294	5.78%
Coarse (N3)	20274	h_3=3.67		0.277	-

The grid convergence index (GCI) method [15] was then employed to assess the convergence and numerical uncertainty of these results, for which the apparent order (p) had to be determined first.

The p of the method was determined using Eqs. (10) to (12):

$$p = \frac{1}{\ln(r_{21})} |\ln|\varepsilon_{32}/\varepsilon_{21}| + q(p)| \tag{10}$$

with

$$q(p) = \ln\left(\frac{r_{21}^{p} - s}{r_{32}^{p} - s}\right) \tag{11}$$

and

$$s = 1 \cdot \text{sgn}(\varepsilon_{32}/\varepsilon_{21}) \tag{12}$$

where $\varepsilon_{32}=\phi_3-\phi_2$, and $\varepsilon_{21}=\phi_2-\phi_1$

To compute the GCI, the following parameters were evaluated, namely the extrapolated values, Eq. (10), approximate relative error, Eq. (11), extrapolated relative error, Eq. (12), and GCI for the fine grid, Eq. (13):

$$\phi_{ext}^{21} = \left(r_{21}^{p}\phi_1 - \phi_2\right)/\left(r_{21}^{p} - 1\right) \tag{13}$$

$$T_a^{21} = \left|\frac{T_1 - T_2}{\phi_1}\right| \tag{14}$$

$$\phi_{ext}^{21} = \left|\frac{\phi_{ext}^{12} - \phi_1}{\phi_{ext}}\right| \tag{15}$$

$$GCI_{\text{fine}}^{21} = \frac{1.25 e_a^{21}}{r_{21}^{p} - 1} \tag{16}$$

Using the computed maximum temperature for each grid in Table 3, the extrapolated values implied that the infinite number of the grid was 0.309. The GCI also indicated that the mesh was well-converged in terms of the relative error of 2.33% and GCI of 3.50% for the fine mesh. Therefore, the fine mesh of 347,489 element number will be used for further simulation study as it provides accurate result with error less than 5%.

Table 3. The parameters of the grid convergence index (GCI).

Parameter	Value
Apparent order (p)	2.00
Extrapolated values (ϕ_{ext}^{21})	0.309
Approximate relative error (e_a^{21})	2.33%
Extrapolated relative error (e_{ext}^{21})	2.72%
Fine-grid convergence index (GCI_{fine}^{21})	3.50%

3. Results and Discussion

Several results were evaluated in this section, including the T over the timestep, the vorticity distribution, and the C_p of both the clean and plain flap aerofoils at various TSRs.

3.1. Vorticity distribution different TSR

Figure 3 shows the contours of the vorticity magnitude around the aerofoil at TSR = 1.5. In this case, the regions of high vorticity were primarily located near the trailing edge of the aerofoil. These areas indicated where the flow separated from the aerofoil, creating strong vortices. The wake behind the aerofoil exhibited alternating regions of high and low vorticities, indicating vortex shedding. The vortices were shed in a regular pattern.

Similar to the clean aerofoil, high vorticity regions were observed near the trailing edge and around the flap. These regions indicated strong vortex formation due to the increased complexity of the flow around the flap. The wake behind the aerofoil with the flap exhibited a more pronounced and complex vortex-shedding pattern compared to the clean aerofoil. The vortices were larger and more numerous, indicating that the flap significantly impacted the flow dynamics. Overall, at lower TSRs, the clean airfoil shows prominent vortex shedding, indicating flow separation and dynamic stall, which are well-documented inefficiencies in VAWTs [3]. The addition of flaps improves flow attachment by reducing trailing edge separation and modifying vortex behaviour, as supported by Jin et al. [11].

Figure 4 shows the contours of the vorticity magnitude of the plain flap installed on the aerofoil at TSR = 2.0. The wake behind the aerofoil showed a distinct vortex-shedding pattern, with vortices regularly spaced and alternating between high and low vorticity regions. This regular pattern indicated a periodic shedding process and suggested stable aerodynamic behaviour.

Compared to the lower TSR of 1.5, the vorticity at TSR = 2.0 was more consistent and stable, reflecting enhanced aerodynamic efficiency and more predictable flow behaviour around the aerofoil. Meanwhile, for the plain flap aerofoil, the wake behind the aerofoil showed a more pronounced and complex vortex-shedding pattern compared to the clean aerofoil. The wake extended further downstream with alternating high and low vorticity regions, showing the sustained rotational motion induced by the flap. The interaction between these vortices created a more complex turbulent wake structure than that of the clean aerofoil.

For the vorticity magnitude of the clean aerofoil at TSR = 2.5 (Fig. 5), the aerofoil created a clear and repeated pattern of swirling air behind it. These swirls were well-defined and alternated between strong and weak areas, indicating a steady and recurring process. This regular pattern suggested that the aerofoil operated efficiently at this TSR. The continuous presence of vortices indicated optimal aerodynamic performance and efficient lift generation. Compared to the lower TSRs of 1.5 and 2.0, the vorticity at TSR = 2.5 was more consistent and stable, indicating improved aerodynamic efficiency and a more predictable flow behaviour around the aerofoil.

Meanwhile, the wake behind the aerofoil with the flap displayed a noticeable and complex vortex-shedding pattern. The vortices were larger and more numerous compared to those of the clean aerofoil, showing that the flap significantly influenced the flow dynamics. The plot demonstrated several swirling spots that merged as they moved downstream. This interaction suggested that the flap added extra rotational energy to the flow, making the wake more energetic but less stable. The shedding of vortices created a more complex and turbulent wake compared to

the clean aerofoil. This increased turbulence can impact aerodynamic performance, possibly improving lift but also increasing drag due to the added rotational energy in the flow.

Figure 6 shows the contours of the vorticity around the aerofoil at TSR = 3.0. The swirling pattern continued downstream with clear spinning structures, but they became less defined as they moved farther from the aerofoil. The persistence of these vortices showed a sustained rotational motion, but the diffusion indicated energy loss and reduced aerodynamic efficiency. The contour plot showed a clear vortex-shedding pattern, but the vortices were spread out more compared to the lower TSRs. The swirling motion was less organised and more dispersed at TSR = 3.0 compared to TSR = 2.5, indicating less efficient aerodynamics and more complex airflow around the aerofoil.

Finally, for the plain flap aerofoil, the swirling pattern continued downstream with clear vortex structures. These vortices showed a persistent ongoing rotation, but they became more spread out as they moved away from the aerofoil, signifying energy loss. The plot displayed many areas of strong swirls merging as they moved downstream. This suggests there was extra rotational energy in the flow, making the wake more turbulent and less steady. Despite this, the aerodynamic performance, as reflected in the T values, did not significantly improve, indicating that TSR = 3.0 was not optimal for either configuration, though it yielded better results compared to the clean aerofoil.

Nevertheless, at higher TSRs, while the flaps introduce additional complexity in the wake structure, they contribute to better control of vortex shedding, stabilizing torque output and improving aerodynamic performance. These observations align with findings by Zhang et al. [13], who showed that trailing edge modifications can optimize flow dynamics in VAWTs. In summary, the integration of plain flaps on the trailing edge of the turbine blades significantly influences the flow dynamics by mitigating flow separation and enhancing reattachment. The interaction between the flap and surrounding airflow modifies the vortex shedding pattern, resulting in a more controlled wake structure.

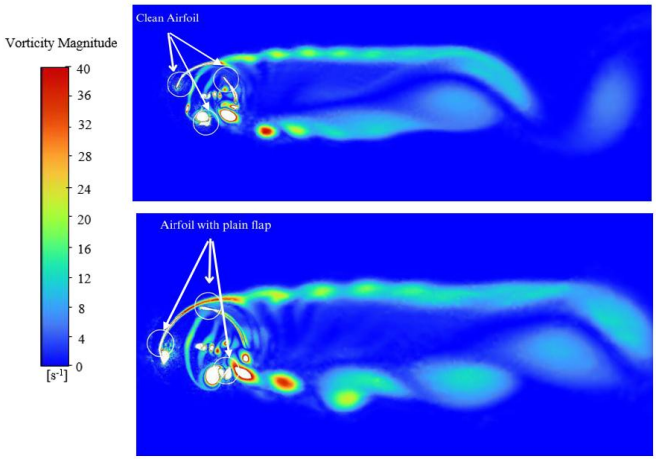

Fig. 3. The vorticity magnitude of the clean aerofoil (top) and plain flap aerofoil (bottom) at TSR=1.5.

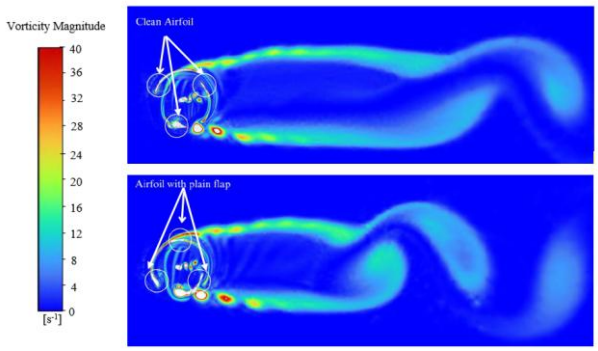

Fig. 4. The vorticity magnitude of the clean aerofoil (top) and plain flap aerofoil (bottom) at TSR=2.0.

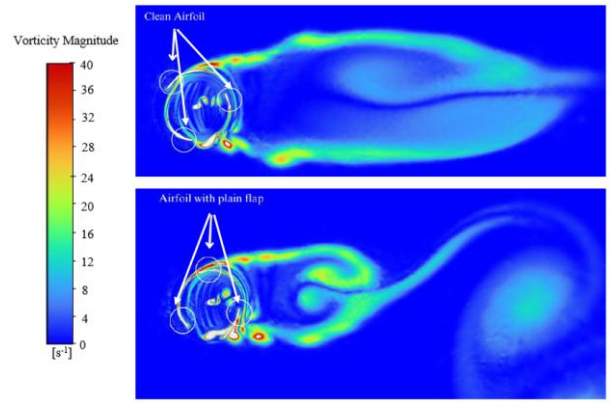

Fig. 5. The vorticity magnitude of the clean aerofoil (top) and plain flap aerofoil (bottom) at TSR=2.5.

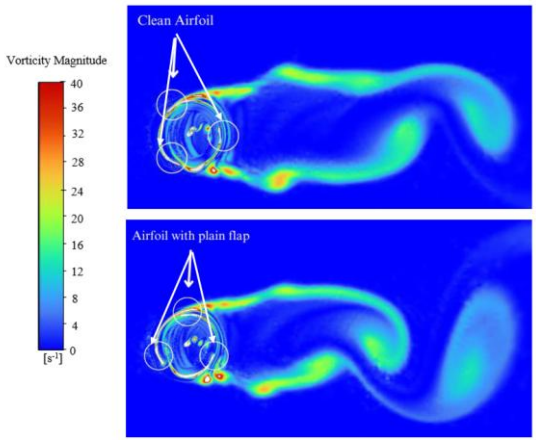

Fig. 6. The vorticity magnitude of the clean aerofoil (top) and plain flap aerofoil (bottom) at TSR=3.0.

3.2. Torque (T), wind power (p) and pressure coefficient (c_p)

Figures 7 and 8 show the average torque measured for the 360 timesteps for both the clean and plain flap aerofoils, respectively at different TSRs. The plain flap aerofoil consistently showed higher torque fluctuations than the clean aerofoil at all TSRs. This indicated that the flap increased the aerodynamic forces, leading to a higher torque but also more significant unsteady effects. The waveforms for the clean aerofoil became more regular and sinusoidal as the TSR increased, indicating more stable aerodynamic performance at higher TSRs.

For the aerofoil with the flap, while the waveforms also became more regular at higher TSRs, the fluctuations were more pronounced. The increased torque fluctuations with the flap suggested that the flap enhanced the aerodynamic forces, potentially increasing the lift but at the cost of higher unsteady forces. At higher TSRs, the flap still had a noticeable impact, although the aerodynamic forces became more stable, suggesting that the influence of the flap was more significant at lower TSRs.

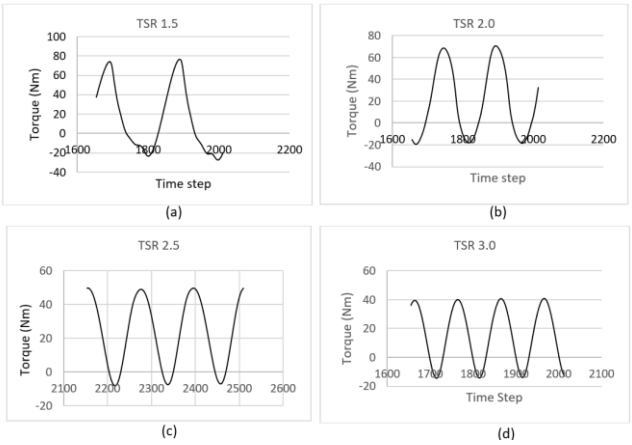

Fig. 7. The torque of the clean aerofoil at the last 360 timesteps at different TSRs.

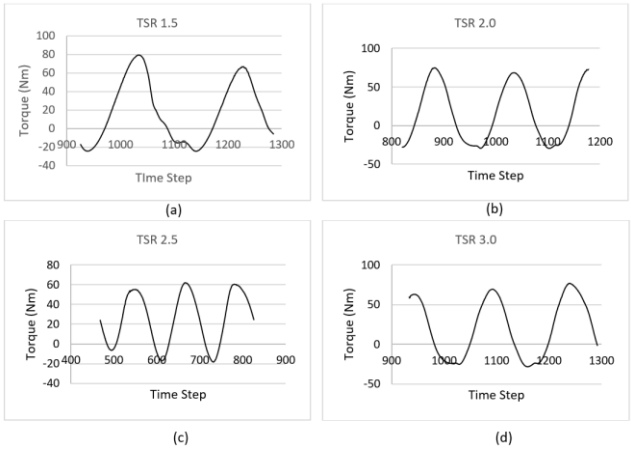

Fig. 8. The torque of the plain flap aerofoil at the last 360 timesteps at different TSRs.

The torque values in Figs. 7 and 8 were the averages for all the 360 timesteps, which were then used to calculate the wind turbine power and C_p (Eq. (6)). Table 4 presents the calculated data. As can be seen, the torque, power, and C_p increased for all TSRs, indicating that the turbine with the flap was more efficient in converting the kinetic energy of the wind into mechanical energy at all operating ranges. It is noteworthy that although the C_p was higher at TSR = 2.5, it had the lowest improvement with the incorporation of the plain flap. Furthermore, for both aerofoils, as the TSR got higher, the C_p was lower. This was expected to happen. Since the tips were faster than the relative wind, there could have been a loss of aerodynamics at the tips, as proven by the increase in vortex shedding for TSR = 3.0 (Fig. 6).

Also seen in Table 4, the observed 10-20% improvement in power coefficient (Cp) varies across the tested TSRs, with the most significant benefits occurring at lower TSRs (e.g., 19.42% at TSR = 3.0). This variation can be attributed to the interaction between the flap and airflow dynamics at different rotational speeds. At lower TSRs, the blades experience higher angles of attack, leading to pronounced flow separation and dynamic stall. However, at higher TSRs, where the relative velocity between the blade and wind is higher, the flap's contribution diminishes as flow separation is naturally reduced and drag induced by the flap becomes more pronounced.

Table 4. The torque (*t*), wind turbine power (*p*), and power coefficient (c_p) of the clean and plain flap aerofoils at different tip speed ratios (TSRs)

TSRs	Clean Airfoil			Plain Flap Airfoil			% *Cp* increase
	Average Torque (T)	Wind Turbine Power (P)	*Cp*	Average Torque (T)	Wind Turbine Power (P)	*Cp*	
1.5	15.797	189.564	0.124	18.221	218.652	0.143	15.32%
2.0	18.578	297.248	0.194	21.629	346.064	0.226	16.49%
2.5	23.040	460.812	0.301	25.298	505.968	0.331	9.97%
3.0	15.482	371.568	0.242	18.467	443.232	0.289	19.42%

4. Conclusions

This study demonstrated that the integration of flaps into VAWTs can significantly enhance their aerodynamic performance and overall energy output. Through comprehensive CFD simulations, it was found that the use of flaps consistently improved the power coefficient of the turbine by 10%-20% compared to a clean aerofoil configuration, depending on the TSR.

Additionally, the introduction of flaps led to a more stable and increased torque output, further contributing to the overall efficiency of the turbine. The flaps effectively optimised the angle of attack and mitigated adverse aerodynamic phenomena, such as dynamic stall, by influencing the vorticity patterns around the blades. This not only improved the lift-to-drag ratio but also resulted in higher wind power capture. These findings underscore the potential of flap technology to address some of the inherent inefficiencies in VAWT designs, particularly at lower TSRs where these turbines typically underperform.

While the addition of flaps significantly enhances the C_p and mitigates dynamic stall, potential drawbacks must be considered to provide a balanced perspective. One key trade-off is the increased drag introduced by the flaps, particularly at higher tip speed ratios (TSRs), which may partially offset the efficiency gains.

Future studies should explore methods to minimize drag, such as optimizing flap dimensions or incorporating active control mechanisms, while evaluating the cost-benefit trade-offs of implementing flaps in commercial-scale wind turbines.

Acknowledgement

The authors thank Universiti Teknikal Malaysia Melaka (UTeM) and its Faculty of Technology and Mechanical Engineering for their practical support.

Nomenclature

A_s	Sweep area
C	Chord length
C_P	Power coefficient
D	Rotor/turbine diameter
H	Turbine height
k	Turbulent kinetic energy
N	Grid number
P	Wind Turbine Power
T	Torque
$\boldsymbol{U}$	Velocity vector

Greek Symbols

ρ	Density
ε	Turbulent dissipation rate
ω	Angular velocity

Abbreviations

CFD	Computational fluid dynamics
GCI	Grid convergence index
SST	Shear Stress Transport
TSR	Tip speed ratio
URANS	Unsteady Reynolds-averaged Navier–Stokes equations
VAWT	Vertical axis wind turbine

References

1. Wang, Q.; Ma, P.; Zhao, Z.; and Li, D. (2024). Effects of fluctuating velocity on dynamic stall of vertical axis wind turbine airfoil. *Renewable Energy*, 235,120787.
2. Syawitri, T.P.; Yao, Y.; Yao, J.; and Chandra, B. (2022). Geometry optimisation of vertical axis wind turbine with Gurney flap for performance enhancement at low, medium and high ranges of tip speed ratios. *Sustainable Energy Technologies and Assessments*, 49, 101779.
3. Hao, W.; and Li, C. (2020). Performance improvement of adaptive flap on flow separation control and its effect on VAWT. *Energy*, 213, 118809.
4. Hafidzal, M.H.M.; Mahmood, W.M.F.W.; Manaf, M.Z.A.; Zakaria, M.S.; Saadun, M.N.A.; and Nordin, M.N.A. (2013). Soot particle trajectories of a Di

diesel engine at 18° ATDC crankshaft angle. *IOP Conference Series*: *Materials Science and Engineering*, 50, 012003.

5. Basri, A.A.; Zuber, M.; Zakaria, M.S.; Basri, E.I.; Aziz, A.F.A.; Ali, R.M.; Tamagawa, M.; and Ahmad, K.A. (2016). The hemodynamic effects of paravalvular leakage using fluid structure interaction; transcatheter aortic valve implantation patient. *Journal of Medical Imaging and Health Informatics*, 6(6), 1513-1518.
6. Zakaria, M.S.; Osman, K.; and Abdullah, H. (2013). Greenhouse gas reduction by utilization of cold LNG boil-off gas. *Procedia Engineering*, 53, 645-649.
7. Zakaria, M.S.; Osman, K.; Yusof, A.A.; Hanafi, M.H.M.; Saadun, M.N.A.; and Manaf, M.Z.A. (2014). Parametric analysis on boil-off gas rate inside liquefied natural gas storage tank. *Journal of Mechanical Engineering and Sciences* (*JMES*), 6, 845-853.
8. Hoseinzadeh, S.; Bahrami, A.; Mirhosseini, S.M.; Sohani, A.; and Heyns, S. (2020). A detailed experimental airfoil performance investigation using an equipped wind tunnel. *Flow Measurement and Instrumentation*, 72, 101717.
9. Hoseinzadeh, S.; Sohani, A.; and Heyns, S. (2021). Comprehensive analysis of the effect of air injection on the wake development of an airfoil. *Ocean Engineering*, 220, 108455.
10. Jadallah, A.A.; Farag, S.R.; and Hamdi, J.D. (2018). Performance enhancement of a Darrius 3-bladed wind turbine using convergent-divergent ducting system. *Journal of Engineering Science and Technology*, 13(7), 1891-1904.
11. Jin, X.; Zhao, G.; Gao, K.; and Ju, W. (2015). Darrieus vertical axis wind turbine: Basic research methods. *Renewable and Sustainable Energy Reviews*, 42, 212-225.
12. Hao, W.; Bashir, M.; Li, C.; and Sun, C. (2021). Flow control for high-solidity vertical axis wind turbine based on adaptive flap. *Energy conversion and management*, 249, 114845.
13. Zhang, L.; Gu, J.; Hu, K.; Zhu, H.; Miao, J.; Li, X.; Ma, D.; Mi, Y.; and Wang, Z. (2021). Influences of trailing edge split flap on the aerodynamic performance of vertical axis wind turbine. *Energy Science & Engineering*, 9(1), 101-115.
14. Sparrow, E.M.; Abraham, J.P.; and Minkowycz, W.J. (2009). Flow separation in a diverging conical duct: Effect of Reynolds number and divergence angle. *International Journal of Heat and Mass Transfer*, 52(13-14), 3079-3083.
15. Celik, I.B.; Ghia, U.; Roache, P.J.; Freitas, C.; Coleman, H.; and Raad, P.E. (2008). Procedure for estimation and reporting of uncertainty due to discretization in CFD applications. *Journal of fluids Engineering*, 130(7), 078001.